WILEY-VCH

DOI: 10.1002/adma.202106280

Article type: Communication

Homologous bromides treatment for improving the open-circuit voltage of perovskite solar cells

Yong Li, Weidong Xu, Nursultan Mussakhanuly, Yongyoon Cho, Jueming Bing, Jianghui Zheng, Shi Tang, Yang Liu, Guozheng Shi, Zeke Liu, Qing Zhang, James R. Durrant, Wanli Ma*, Anita W. Y. Ho-Baillie and Shujuan Huang*

Y. Li, N. Mussakhanuly, Dr. J. Bing, Dr. J. Zheng, S. Tang, Prof. A. W.Y. Ho-Baillie, Prof. S. Huang
Australian Centre for Advanced Photovoltaics, School of Photovoltaic and Renewable Energy Engineering, University of New South Wales (UNSW), Sydney 2052, Australia

W. Xu, Prof. J. R. Durrant

Department of Chemistry and Centre for Processable Electronics, Imperial College, London, W12 0BZ, UK.

Y. Cho

Division of Materials Science, Nara Institute of Science and Technology, Ikoma, Nara

630-0192, Japan

Dr. J. Bing, Dr. J. Zheng, S. Tang, Prof. A. W.Y. Ho-Baillie

School of Physics and University of Sydney Nano Institute, The University of Sydney, NSW 2006, Australia

Y. Liu, Dr. G. Shi, Prof. Z. Liu, Prof. W. Ma

Jiangsu Key Laboratory for Carbon-Based Functional Materials and Devices Institute of Functional Nano & Soft Materials (FUNSOM), Soochow University, Suzhou 215123, China

Dr. Q. Zhang

Vacuum Interconnected Nanotech Workstation, Suzhou Institute of Nano-Tech and Nano-Bionics, Chinese Academy of Sciences, Suzhou 215123, Jiangsu, China

Prof. J. R. Durrant

SPECIFIC IKC, College of Engineering, Swansea University, Bay Campus, Fabian Way, Swansea SA1 8EN, UK

Prof. S. Huang

School of Engineering, Macquarie University, Sydney 2109, Australia

*Correspondence: shujuan.huang@mq.edu.au (S. H.)

Abstract

Solution-processed organic-inorganic mixed halide perovskite solar cells have achieved rapid improvements in power conversion efficiency (PCE). However, it is imperative to minimise voltage deficit (W_{oc}=E_g/q-V_{oc}) for the state-of-the-art cells for their PCE to approach the theoretical limit. Herein, we report the strategy of depositing homologous bromide salts on the perovskite surface to achieve a surface and bulk passivation for the fabrication of solar cells with high open-circuit voltage. A W_{oc} of 0.39 V (V_{oc} =1.24 V) in 1.63 eV bandgap (determined by EQE) perovskite device (PCE= 22.1%) and a W_{oc} of 0.38 V (V_{oc} =1.18 V) in 1.56 eV bandgap perovskite device (PCE= 23.7%) are demonstrated on 0.159 cm^2. Meanwhile, we also achieved an efficiency of 21.8% for a large area device of 1×1 cm^2. Distinct to the conclusions given by previous works that the homologous bromides such as FABr only react with PbI_2 to form a large bandgap perovskite layer on top of the original perovskite, our work finds that the bromide also penetrates the perovskite film and

passivates the perovskite in the bulk. This is confirmed by the small bandgap enlargement observed by absorbance and photoluminescence (PL), bromide element ratio increasing in bulk by time-of-flight secondary ion mass spectrometry (TOF-SIMS) and depth-resolved X-ray photoelectron spectroscopy (XPS). Furthermore, a clear suppression of non-radiative recombination in the perovskite device was confirmed by a variety of characterisations. The best non-encapsulated device with homologous bromide passivation maintained 97% of its initial efficiency after 2500 hours of ambient storage and 59% after 520 hours of thermal stability test at 85°C. Our work provides a simple and universal way to reduce the W_{oc} of single-junction perovskite solar cells and it would also shed light on developing other high performance optoelectronic devices, including perovskite-based tandems and light-emitting diodes (LEDs).

Introduction

Performance of solution-processed organic-inorganic mixed halide perovskite solar cells have improved tremendously to a PCE of 25.5% independently certified in 2021 due to their excellent optoelectronic properties,[1-3] ease of solution-processing and excellent defect tolerance. [4-6] At present, stable perovskite materials that are used in the state-of-the-art cells have a bandgap of around 1.6 eV. At this bandgap, the maximum power conversion efficiency (PCE) is 30% according to Shockley-Queisser (SQ) efficiency limit, with a short-circuit current (J_{sc}) of 25 mA/cm^2 and an open-circuit voltage (V_{oc}) of 1.3 V. [7] However, the best-performing cells at this bandgap have achieved a

J_{sc} ~24 mA/cm^2 and a V_{oc} of ~ 1.15 V, over 96% of its J_{sc} limit but just 88% of V_{oc} SQ limit.[8-9] This indicates that there is an opportunity for V_{oc} improvement, by reducing the voltage deficit W_{oc} of perovskite solar cells.

The origin of the W_{oc} is mainly ascribed to the generation of non-radiative recombination centres formed during the perovskite film fabrication process, especially at the interfaces between the perovskite and the electron- and/or hole- transport layers as well as the perovskite grain boundaries. Recently, strategies have been developed to improve the quality of the perovskite surface by using organic materials with functional groups, such as poly(methyl methacrylate) (PMMA) ,[10-11] phenyl-C61-butyric acid methyl ester (PCBM), [12-15] thiophene and pyridine. [16,17] These materials have electron rich functional groups such as carboxyl or amino group which can form the Lewis acid-base adduct and passivate the under-coordinated ions on the perovskite surface and grain boundaries.[18] Furthermore, halide materials such as guanidinium bromide (GABr)[19], phenethylammonium iodide (PEAI),[20] n-hexyl trimethyl ammonium bromide (HTAB)[21] and n-octylammonium bromide (C_8Br)[22] have also been used for passivation purposes for perovskite cells achieving PCE of above 22.6% up to 23.5%. It is believed that the passivation provided by bromide is via the formation of a larger bandgap but thin perovskite layer on the top of the perovskite resulting in an increase in voltage output without comprising the current output.[23-27] For example, methylammonium bromide (MABr) has been used for $MAPbI_3$ cell achieving 19.1% efficiency and improved V_{oc} from 1.05 V to 1.12 V.[23] MABr has also been used for $(FA_{0.83}MA_{0.17})_{0.95}Cs_{0.05}Pb(I_{0.83}Br_{0.17})_3$ (where FA = formamidinium) and $FAPbI_3$ perovskites cells with improved device efficiency and light stability.[24-26] FABr has been used in $(FAPbI_3)_{0.85}(MAPbBr_3)_{0.15}$ perovskite cell achieving an efficiency of 21.3% and improved V_{oc} from 1.10 V to 1.16 V.[27] All the above mentioned studies only used one type bromide

passivation materials and there lacks deep understanding on the homologous bromide passivation mechanism such as where the bromide located and how the bromide influences perovskite bandgap and device performance.

Here, for the first time, we systematically investigate the use of various homologous bromide salts, including FABr, MABr, and PEABr to passivate triple-cation mixed halide perovskite with a composition of $Cs_{0.05}FA_{0.80}MA_{0.15}Pb(I_{0.85}Br_{0.15})_3$ and a bandgap of 1.63 eV (determined from EQE) by the facile surface-deposition technique. The champion cell achieved a very high V_{oc} of 1.24 V (W_{oc}= 0.39 eV) and an efficiency of 22.1%. Different to previous works that reported the reason for performance improvement being surface passivation provided by the bromide rich surface layer, we found that the bromide salts such as the FABr can penetrate the perovskite film, change the chemical and physical properties both on perovskite surface and in bulk. This is confirmed by the small bandgap enlargement observed by UV-*vis* absorbance, steady-state PL and continuous wave PL, bromide element ratio increasing both on perovskite surface and in perovskite bulk by normal XPS, TOF-SIMS and depth-resolved XPS. Furthermore, results of device open-circuit to short-circuit photoluminescence quenching efficiency ($PLQE_{OC\text{-}SC}$), light-dependent PL and voltage-dependent electroluminescence (EL) measurements of complete perovskite devices confirmed that non-radiative recombination is greatly suppressed after bromide surface treatment. The treatment also improved device stability, the most stable non-encapsulated perovskite device after bromide treatment maintained 97% of its initial efficiency after 2500 hours of ambient (average 65% relative humidity) storage and 59% after 520 hours of thermal stability test at 85°C. In order to check the universality of the homologous bromide passivation, we further applied this passivation technique on a 1.56 eV bandgap perovskite with the composition of $Cs_{0.05}FA_{0.80}MA_{0.15}Pb(I_{0.95}Br_{0.05})_3$ and

achieved an efficiency of 23.7% and V_{oc} of 1.18 V (W_{oc} = 0.38 V), and $MAPbI_3$ perovskite (E_g= 1.60 eV) device with an efficiency of 21.4% and V_{oc} of 1.16 V.

Our work provides a simple and efficient surface treatment using homologous bromides for bulk passivation to reduce non-radiative recombination in the perovskite device, and the demonstrated strategy can be implemented universally to reduce the W_{oc} of different perovskite bandgap and systems. This will also be useful for increasing the performance of large bandgap perovskite and multi-junction perovskite-based tandem solar cells in future works.

Result and discussion

Triple cation mixed-halide perovskites (e.g., $Cs_{0.05}FA_{0.80}MA_{0.15}Pb(I_{0.85}Br_{0.15})_3$) used for solar cell fabrication have demonstrated high efficiency, stability and reproducibility,[28,29] compared to the mono-cation perovskites such as $MAPbI_3$,[30,31] $FAPbI_3$[32,33] and $CsPbI_3$.[34-36] In this work, triple cation mixed-halide perovskites were fabricated by a solution processed one-step antisolvent method, as shown in Figure 1. Details of the fabrication can be found in the Experimental section in the Supplemental Information. For the homologous bromides surface treatment (Figure 1a), the fabricated perovskite films were first cooled down to room temperature before the deposition of bromide salts (dissolved in isopropanol (IPA)) by spin-coating on the perovskite surface followed by an anneal at 100 °C for five minutes. Different bromide salts, namely FABr, MABr and PEABr were then used for surface treatment. Although CsBr was trialled, it was difficult to be dissolved in the regular IPA or chlorobenzene (CB) solvents (Figure S1) and was therefore not investigated in this work.

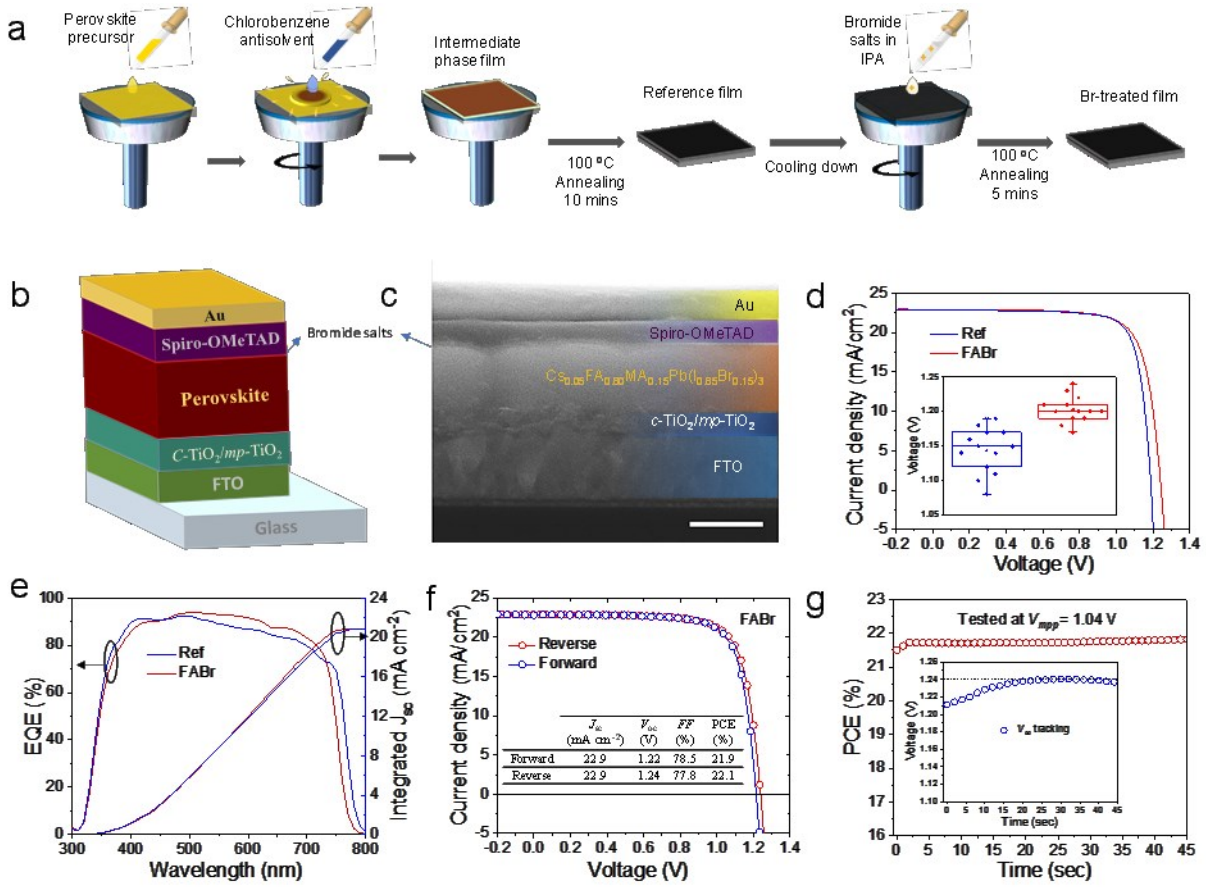

Figure 1. Bromides surface treatment for perovskite solar cells. a) One-step anti-solvent perovskite film deposition including the homologous bromides treatment process using bromide salts in IPA. b) Schematic of the perovskite device structure and c) Cross-sectional scanning electron microscopy (SEM) image of a completed perovskite solar cell, scale bar is 500 nm. d) The best efficiency for the reference and FABr treated perovskite solar cells, inserted the V_{oc} distribution. e) The external quantum efficiencies (EQE) and the integrated J_{sc} of the corresponding devices. f) The forward and reverse scans of current-density vs voltage (*J-V*) curves of the best performing 1.63 eV bandgap perovskite cell after FABr treatment. g) Steady-state efficiency of the FABr treated device, tested at V_{mpp} of 1.04 V and inserted the V_{oc} tracking for 45 seconds.

Table 1. The performance of devices before and after various bromide surface treatments, the highest values are included in brackets as well.

	J_{sc} (mA cm^{-2})	V_{oc} (V)	FF (%)	PCE (%)
Reference	22.5±0.8(23.1)	1.15±0.04(1.19)	77.3±0.3(0.80)	19.8±0.8 (20.9)
MABr	22.3±0.6(22.8)	1.17±0.02(1.21)	77.5±0.2(0.79)	20.5±0.4 (21.4)
FABr	22.5±0.7(23.0)	1.19±0.03(1.24)	78.0±0.1(0.80)	21.5±0.5 (22.1)
PEABr	22.1±1.0(22.8)	1.11±0.02(1.13)	74.0±0.2(0.76)	18.7±0.9 (19.5)

We first fabricated perovskite solar cells (device structure of FTO/compact TiO_2 (*c*-TiO_2)/mesoporous TiO_2 (*mp*-TiO_2)/$Cs_{0.05}FA_{0.80}MA_{0.15}Pb(I_{0.85}Br_{0.15})_3$/Spiro-OMeTAD/Au) with and without surface treatments (Figures 1b-c). Their PV parameters are summarized in Table 1. Both MABr and FABr treated devices show improved efficiencies and V_{oc} which is consistent with previous reports.[23-27] The performance of PEABr treated devices, on the other hand, drops. Figures 1d-g show the photovoltaic performances of the best devices. We also investigated the V_{oc} distribution, the external quantum efficiency (EQE), hysteresis, steady-state efficiency and V_{oc} tracking. Our best FABr passivated device reached an efficiency of 22.1% under reverse scan with a superior stabilized open-circuit voltage of 1.24 V (W_{oc} = 0.39 V) and a steady-state PCE of 21.7% (Figure 1d and 1g). It is also worth noting that our reference sample only achieved a V_{oc} of 1.19 V (W_{oc} = 0.44 V), representing the reduced W_{oc} after the homologous bromide treatment. In addition, minimum hysteresis was measured for both non-passivated and passivated perovskite devices. (Figure 1f and Figure S2) The bandgap of the solar cell with and without FABr treatment determined by the

differentiated EQE in Figure S25b is 1.63 eV and 1.61 eV, respectively. The V_{oc} distribution for the reference and FABr treated cells in Figure 1d represents a W_{oc} loss of only 0.39 V for a 1.63 eV bandgap perovskite solar cell, such a superior V_{oc} is amongst the highest of perovskite solar cells reported with the similar bandgaps (Table S1). As can be found in our EQE in Figure 1e, the FABr treatment causes a notable blue shifted absorption threshold while the increased EQE in the visible region compensates the current loss due to enlarged bandgap as indicated by the integrated J_{sc} of the corresponding devices. As the blue shifted EQE cannot be only explained by the homologous bromide salt FABr formed a large bandgap layer on top of the original lower bandgap perovskite, so the whole bandgap of the perovskite must be changed both at the surface and bulk.

To gain insight into the mechanisms underpinning the device performance improvement and the bandgap enlargement observed after the homologous bromide treatment, various characterisations were performed. XPS characterisation was firstly conducted on the reference and FABr treated films to further understand the chemical effect of the FABr treatment on the surface. While the reference and FABr treated films show the similar responses for whole XPS spectra (Figure S3a), there are changes in the Pb 4*f*, I 3*d* and Br 3*d* peaks after FABr surface treatment as shown in Figure 2a-c. The fact that the C 1*s* peaks in both films are identical (Figure S3b) suggests that changes in Pb, I and Br peaks observed did not come from the measurement errors. It is found that both Pb 4*f* and Br 3*d* peaks for FABr treated sample shifted to lower binding energy (by ~ 0.5 eV) which are the result of the reaction between FABr and PbI_2, thereby changing the chemical surroundings of the Pb and Br elements. The two shoulder Pb 4*f* peaks located at lower binding energies at 136.8 eV and 141.6 eV are associated with the low oxidation state, suggesting the presence of metallic Pb impurities in the reference film. The metallic Pb impurities can be a key defect in non-FABr treated perovskite

films.[37] The two main peaks of Pb 4f were also slightly reduced after FABr treatment which may be due to the addition of FABr on the surface reducing Pb concentration on the perovskite surface. Likewise, the reduced I 3*d* peak after the FABr treatment in Figure 2c suggests reduced percentages of I. This can be the result of a combined effect from reduced PbI_2 (reacted with FABr) as well as increased bromide in the film from the bromide salt surface treatment. Calculated atom ratios of Br in the reference and FABr surface-treated perovskite films are shown in Figure 2d and Table S2 based on depth-resolved XPS profiles shown in Figure S4. The Br/Pb ratio for FABr passivated film is twice that of the non-treated film on the perovskite surface. Furthermore, from Table S2, Br/(Br+I) ratio in the reference film was only 9.3% well below the value of 15% used in perovskite precursor mixing, showing the potential of the bromide vacancies being generated for the reference perovskite film after annealing. However, the Br/(Br+I) ratio increased substantially to 19.8% after FABr treatment, suggesting a higher Br concentration at the surface.

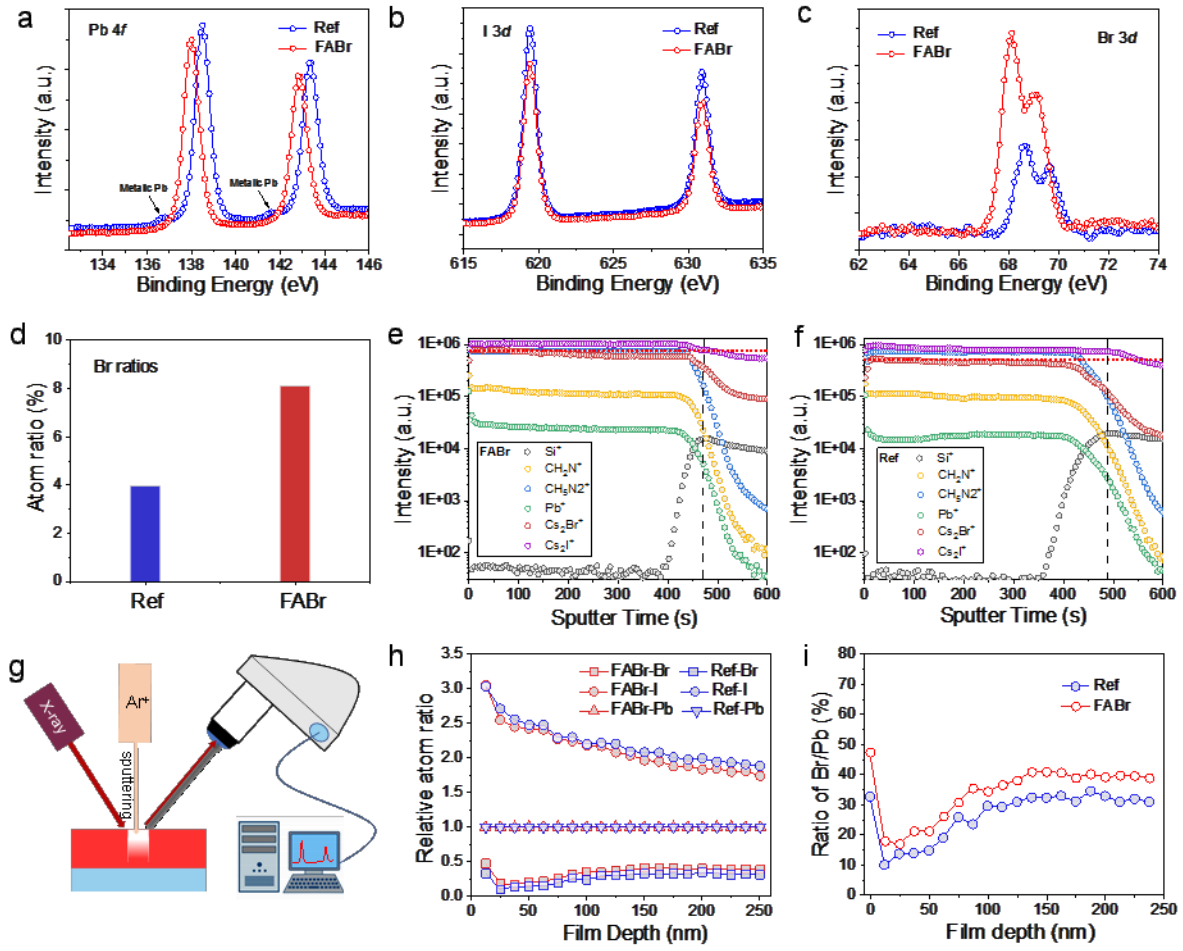

Figure 2. Chemical characterisation of perovskite film before and after FABr treatment. XPS scans for a) Pb 4*f*, b) I 1*s*, and c) Br 3*d*, respectively. d) Bromide atomic percentages at the perovskite surface calculated from XPS spectra. e-f) TOF-SIMS for perovskite reference (e) and FABr treated (f) films on glass. Noted the back dots line represents the interface of the perovskite thin film and glass substrate. g) The schematical illustration of the mechanism of depth resolved XPS characterisation. h) The elements profiles for Pb, I and Br from depth resolved XPS and i) Br/Pb ratios at different depths for the reference and FABr treated perovskite films.

In order to assess how deep the additional bromine can penetrate into the original perovskite film, we further performed the TOF-SIMS for perovskite film on glass and depth-resolved XPS profiles

(schematic mechanism shown in Figure 2g) at different Ar ion etching depths for the reference and FABr treated films on glass. The distribution of all elements in perovskite film is similar when comparing the TOF-SIMS results in Figure 2e-f. However, the Cs_2Br^+ (which represents Br^+ as we used the Cs source) signal intensity marked with a red dot line in FABr treated film (7.9×10^5) is higher than that of the reference film (5.0×10^5) from the top surface to the perovskite bottom, indicating the improvement of bromine concentration is throughout the perovskite. Furthermore, the XPS depth-resolved profiles shown in Figure 2h-i suggest the Br/Pb ratios for FABr treated film at different depths are higher than the reference perovskite film which can be attributed to the additional bromide introduced by FABr treatment. It is notable that for our $Cs_{0.05}FA_{0.80}MA_{0.15}Pb(I_{0.85}Br_{0.15})_3$ perovskite precursors, the Br/Pb should be around 0.45 while Br/Pb ratio in the reference sample estimated by XPS is only around 0.15-0.20 at the top surface and 0.30 at the bulk. After the FABr treatment, the value increased to 0.20-0.30 at the top surface and 0.40 at the bulk. Our results indicate the significant bromine loss is not only limit to the perovskite surface but also to the perovskite bulk. The homologous FABr treatment can offset the loss by providing additional bromine elements. Overall, both the TOF-SMS results and the depth-resolved XPS profile results suggest that bromide surface treatment not only increases the halide amount at the top surface but also within the perovskite bulk. We believe this could be the reason of the enlarged bandgap of FABr treated samples.

We further investigated the perovskite morphology, crystallinity and the optical property changes of the perovskite before and after bromide treatment. The SEM was measured for the perovskite films before and after various bromide surface treatments to compare the morphology changing.

Results are shown in Figure 3a-d and Figure S5 at 1 μm and 3 μm size scales. The SEM results suggest the different bromide treatments did not have a significant impact on the perovskite grain size, while the PbI_2 residual (noticed as the white spots circled in Figure 3a and Figure S5a) on the perovskite film is greatly suppressed after the FABr (cf. Figure 3b and S5b) and MABr (cf. Figure 3c and S5c) treatments. The morphology of the PEABr treated film, on the other hand, became worse as pinholes can be seen in Figure 3d and Figure S5d. This could be one of the reasons that PEABr treated film achieved a lower device performance. The roughness of perovskite films was also evaluated by AFM and the result is shown in Figures S6. The FABr treated film shows the smoothest while the PEABr film is the roughest. For checking the electrical uniformity of the perovskite film, Kelvin probe force microscopy (KPFM) was also employed to characterize the spatial surface potentials of the perovskite films with different bromide salts treatments. Results in Figure S7 show FABr treated film has the most uniform surface potentials which represents the surface chemical/electrical characteristics are the most homogeneous therefore can be a benefit for achieving better device performance. [38] The morphology characterisation by SEM, AFM and KPFM reveal that PbI_2 residual can be significantly reduced by FABr and MABr treatments with reduced surface roughness and improved uniformity.

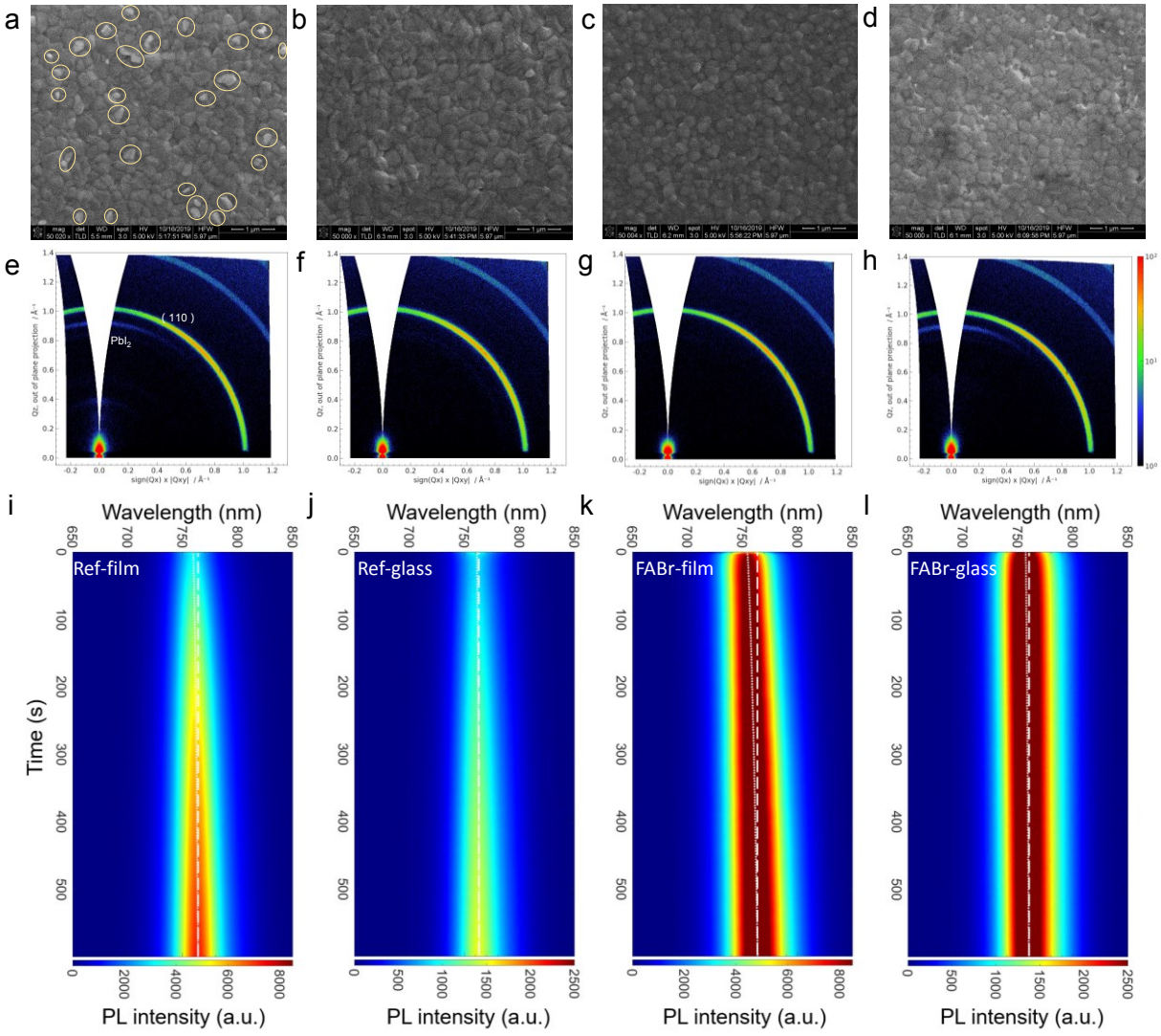

Figure 3. Influence of bromide treatment on perovskite morphology, crystallinity and optical changes. Scanning electron microscopy (SEM) images of the a) reference, b) FABr, c) MABr and d) PEABr surface-treated perovskite film. GIWAXS results (e-h) of the corresponding 1.63 eV bandgap perovskite films with different bromide treatments. CWPL for the perovskite/glass samples without (i, j) and with FABr (k, l) passivation, noted i) and k) are measured from the film side, j) and l) are measured from the glass side.

GIWAX and XRD were measured for perovskite thin films to compare their crystallinity before and after various bromides treatments. For the GIWAX results in Figure 3e-h and Figure S8, the q= 1.0 $Å^{-1}$ (where q= 4πsin (θ)/λ) corresponds to the (110) perovskite main peak while the q= 0.9 $Å^{-1}$ corresponds to hexagonal PbI_2. For XRD results in Figure S9a-b, the peaks at ~14° and 12.5° represent the perovskite (110) phase and the PbI_2 (001) plane,[28] respectively. Both GIWAX and XRD results show a suppression of PbI_2 peak after FABr and MABr passivation. Furthermore, the full width at half maximum (FWHM) values of perovskite (110) peaks were calculated for the reference, FABr, MABr and PEABr treated films which indicate there is no significant change in perovskite crystallinity after the bromide treatment, this is also consistent with the similar perovskite (110) peak intensity in GIWAX and similar grain size in SEM. It is noteworthy that from Figure S9c, the perovskite peak of FABr and MABr treated films shifts slightly to larger diffraction angles, suggesting a reduction in lattice constant due to the bromide elements diffused into the perovskite bulk.[39] Furthermore, the suppressed PbI_2 peak both in XRD and GIWAX is also consistent with the minimized PbI_2 residual in morphology results, confirming the reaction between the bromide salt and the PbI_2.

For investigating the effect of the different bromide treatments on the perovskite optical properties, optical absorbance and steady-state PL spectra were measured. As shown in Figures S10 and Figures S11, MABr and FABr treated films showed a blue shift (by ~10 nm) compared with the reference and PEABr passivated samples, indicating enlarged optical bandgap. This is in accordance with the EQE result in Figure 1f. The intensities of the steady-state PL for FABr and MABr treated samples also greatly increased - almost doubled for MABr and tripled for FABr compared with the reference film (Figure S10b). However, it can be found that the decreased steady state PL peak intensity for the PEABr treated perovskite film, suggesting the increased of the non-radiative

recombination. This could be due to the 2D passivation material PEABr on the perovskite film gradually converted into the $PEA_2Pb(I/Br)_4$ phase during the thermal annealing process.[20] We also measured the absorbance of the FABr-treated perovskites annealed at different temperatures and periods to study how fast the FABr treatment affects the bandgap of the perovskite film. Figure S12 shows that the films' bandgaps increase spontaneously after FABr treatment, even without annealing, indicating the process of bromide penetration or passivation into perovskite bulk proceeded promptly. We further checked the perovskite bandgap changes for repeated FABr treatment (Figures S13) and treated them with different FABr concentrations (Figures S14). The results show that the perovskite bandgap can keep increasing by applying multiple times FABr treatment while the perovskite bandgap reaches a plateau when just increasing the FABr concentration.

CWPL spectroscopy was conducted for perovskite films from the film side and the glass side with the results shown in Figure 3i -l and Figure S15-18. By comparing the CWPL results measured from the film side, it is interesting to find that the CWPL peak of the passivated perovskite red shifted about 10 nm from 755 nm to 764 nm after 10 min illumination, however, there is no obvious peak position change from the glass side. We suppose that the shifted CWPL peak may result from the light-induced bromide ion movement, which is shown in the schematic illustration in Figure S19. Before the CWPL measurement, the bromide distribution is not even and more bromide elements are located at the upper surface of perovskite film due to the surface FABr treatment. When the CWPL measurement starts, the bromide elements on the perovskite surface will diffuse into the bulk under the laser light due to the gradient of bromide concentration, therefore the bandgap at the surface decreases which resulting a slight red shift in CWPL. However, when the light comes from

the glass side, there are almost no bromide gradient at the bottom/glass side so the bromide diffusion will be very slow or even not happen, therefore the perovskite bandgap stays constant. Overall, after the FABr treatment, we can see a much stronger CWPL intensity during the whole measurement period both at the film side and the glass side, suggesting the significant suppression of the non-radiative recombination.

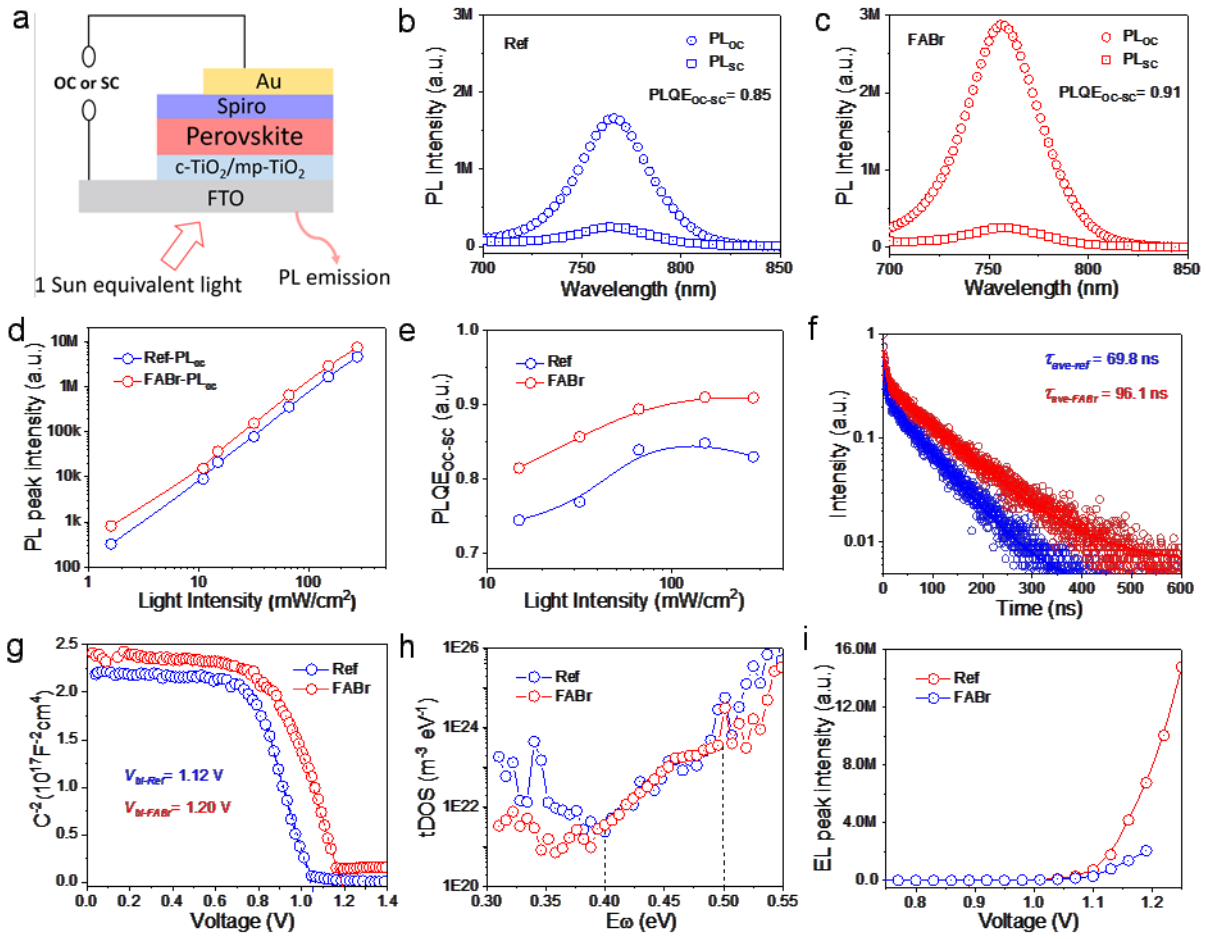

Figure 4. Charge dynamics characterisation for perovskite devices. a) Completing cells being used for open circuit (OC) to short circuit (SC) PL quenching efficiency ($PLQE_{OC-SC}$) measurement. Results of

$PLQE_{OC-SC}$ for the b) reference and c) FABr treated perovskite cells. d) Light-dependent PL measurement of reference and FABr treated devices under open-circuit conditions and e) the calculated result of light-dependent $PLQE_{OC-SC}$. f) Time-resolved photoluminescence (TRPL) results for reference and FABr treated devices. g) Built-in-potentials (V_{bi}) for reference and FABr treated devices obtained by linear fitting Mott-Schottky plots. h) Trap density of states (tDOS) spectra of reference and FABr passivated devices obtained by thermal admittance spectroscopy. The vertical dashed lines divide trap bands with different trap energy depths. i) The electroluminescence (EL) peak intensities as a function of voltage biases for both perovskite devices.

To investigate the effect of homologous bromide treatment on the recombination characteristics of the perovskite cells, we measured the open-circuit-to-short-circuit (OC-to-SC) PL quenching efficiency ($PLQE_{OC-SC} = (PL_{OC} - PL_{SC})/PL_{OC}$) of the devices with and without FABr treatment. The $PLQE_{OC-SC}$ measurement schematics is illustrated in Figure 4a, steady PL spectra were measured under one-sun equivalent illumination to simulate operating conditions under OC and SC conditions. $PLQE_{OC-SC}$ value describes the magnitude of the difference in PL emission intensity between open and short circuit which can be correlated with solar cell performance.[40] As results shown in Figure 4b-c, the FABr treated device has a higher PL intensity under OC condition than the reference device, indicative of the suppressed non-radiative recombination losses. The FABr treated device also exhibited a high open circuit to short circuit PL quenching efficiency, indicating more efficient charge extraction in this device. Light-intensity-dependent PL was also measured for the reference and FABr-treated devices under OC and SC conditions. Results in Figure 4d show that the FABr-treated device has consistently higher PL intensities for all light intensities under OC, indicating suppression of non-radiative recombination and an enlarged quasi-fermi-level-splitting (QFLS) in the device.[41-43]

The light-dependent $PLQE_{OC-SC}$ (Figure 4e) for both devices goes up and then flattens with increasing excitation light intensity, indicative of the competition between charge extraction to the out circuit and recombination in the device, where more charge carriers are extracted rather than recombined under higher fluence illumination. $PLQE_{OC-SC}$ values for FABr-treated devices are higher across the whole light intensity range, revealing improved charge extraction at SC and consistent with the higher EQE observed for this device. The TRPL results in Figure 4f and Table S3 also suggest that FABr treated perovskite exhibit a longer average PL lifetime than the reference perovskite, consistent with the suppressed non-radiative losses. Furthermore, the results of the Nyquist plots obtained from the electrical impedance spectroscopy (EIS) are shown in Figure S20. The middle frequency zone of the Nyquist plot can be dominated by junction capacitance and recombination resistance related to the interfaces between transport materials and perovskite.[44] The larger impedance in the FABr passivated device indicates the improved carrier flow between perovskites and carrier transport layers. The light intensity dependant voltage and light intensity dependant current measurements were also conducted (Supplementary Note 1) with the results shown in Figure S21. A low ideality factor (n=1.04 *vs* n=1.31) for the FABr-treated indicates the trap-assistant Shockley-Read-Hall (SRH) recombination was suppressed in the film. The dark current density-voltage (*J-V*) characteristics of reference and FABr treated devices were also measured with the result shown in Figure S22. The obtained J_0 of the FABr-treated device is three times smaller than that of the reference device, proving shallower defect states existed in the device.[45] Ideality factors (n) were also extracted by estimating the slope of the semilogarithmic *J-V* curve in the diffusion-dominated current region. The reduced ideality factor in dark *J-V* is also consistent with the finding in light intensity dependant voltage measurement.

For elucidating the reduction of W_{oc} in the passivated devices, built-in potentials (V_{bi}) for reference and FABr treated devices are evaluated through Mott-Schottky plot analysis. The detailed measurement method and calculation formula can be found in Supplementary note 2. As shown in Figure 4g, the perovskite device with FABr treatment presents enlarged build-in potential (V_{bi}) which increased from 1.12 V to 1.20 V. The improved V_{bi} will facilitate charge separation and prevent carrier recombination.[46] Furthermore, the space charge limited current (SCLC) measurement was also conducted with the device structure of FTO/TiO_2/perovskite/PCBM/Ag (Figure S23). The corresponding *J-V* results and calculated parameters including trap-filled limit voltage (V_{TFL}), the defect density (N_t) and the mobility (μ) are shown in Table S4. The details of the calculation can be found in Supplementary Note 3. It is found the defect density of perovskite film with FABr passivation was reduced while the mobility doubled compared to the reference perovskite film. For quantifying the trap state of density (tDOS) of the reference and FABr passivated devices, thermal admittance spectroscopy was measured at room temperature. (See Supplementary note 4). The tDOS spectra can be divided into three different trap energy depths, shallow trap states (Band 1, 0.30-0.40 eV), deep trap states (Band 2, 0.4 eV-0.50 eV and Band 3, >0.5 eV), the deeper trap region (band 3, >0.5 eV) can be assigned to defects at the film surface while the density of shallower trap states (0.30-0.40 eV) can be assigned to traps at grain boundaries.[47] By comparing the two tDOS spectra in Figure 4h, the perovskite trap states at deep and shallow regions both decreased significantly after the FABr passivation, suggesting the FABr can not only passivate the perovskite surface but also can passivate the perovskite bulk/grain boundaries. The EL characterisation was measured for the completed cells as a function of bias voltage (from 1.01 V to 1.25 V at a 0.03 V interval), whereby free charges can recombine through radiative recombination as in a light-emitting

diode (LED). As shown in Figure S24 and Figures 4i, the FABr treated cell demonstrates a much higher EL intensity compared to the reference cell when bias voltage over 1.0 V, indicating more efficient radiative recombination happened in this device. It is also found that the FABr treated device can withstand a higher bias voltage (>1.2 V) representing the improved device quality. By combining the results above, we can confirm that non-radiative recombination is largely suppressed upon the introduction of the homologous bromide treatment, and the passivation effect is confirmed not only on the perovskite surface but also inside the perovskite bulk.

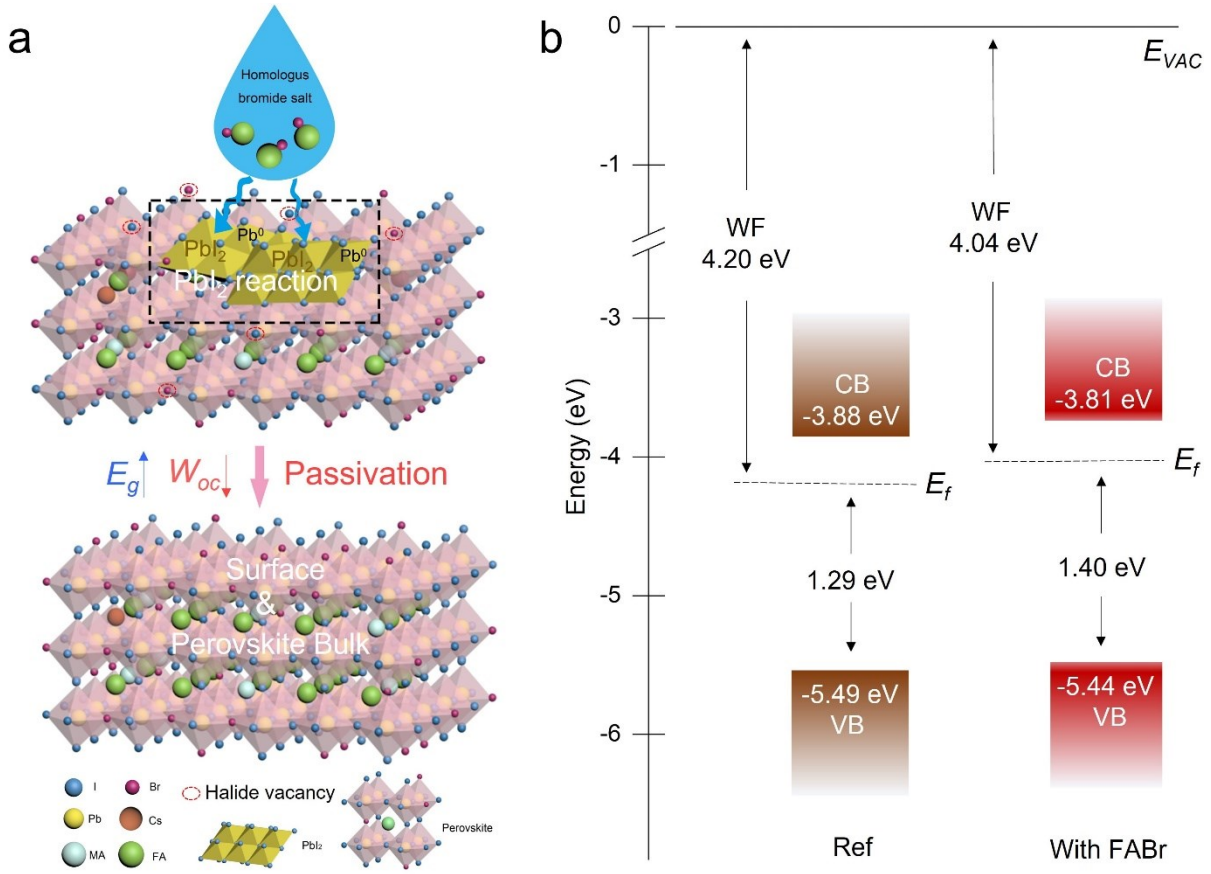

Figure 5. a) Illustration of the proposed homologous bromide passivation mechanism on the perovskite surface as well as in the bulk. b) The corresponding perovskite energy level with and without FABr passivation.

As a summary of our results for our above discussion, the passivation mechanism of the homologous bromide treatment can be schematically illustrated in Figure 5a. The homologous bromides can play two roles, first is to passivate the undercoordinated lead defects (Pb^0 and PbI_2) at the perovskite top surface, second is to diffuse into the perovskite healing the deep level trap states such as the halide vacancies both at the surface and in the bulk.[48]

The ultraviolet photoelectron spectroscopy (UPS) was also conducted for calculating the bandgap energy level of the perovskite film with and without FABr passivation. The helium I_α (hv = 21.22 eV) was used for standardising the binding energy. The UPS spectra edge regions in Figure S25a show that the Fermi level (E_f) is located at 1.29 eV and 1.40 eV on top of the valence band maximum (VBM) for reference film and FABr modified film, respectively. The bandgap of the complete devices deviated from the EQE measurement is shown in Figure S25b, the calculated bandgap for the pristine and passivated films are 1.61 eV and 1.63 eV, respectively. The VBM for reference and passivated films are obtained by fitting the photoelectron yield spectroscopy (PYS) results in Figure S25c-d. By combining the parameters obtained from the UPS, PYS and EQE characterisation, the summarised energy level diagram of the reference and the passivated perovskite is shown in Figure 5b. The Femi level (E_f) for the perovskite film with FABr passivation is witnessed with a shift of 110 meV toward the conduction band minimum (CBM) compared to the reference sample, indicating a more n-type nature for the FABr passivated film. Recent studies have shown this may be attributable to the change of the surface termination since the additional organic cation passivation layer was introduced, a higher possibility of recombination events would be terminated by organic halide which also would be helpful to reduce the deep energy level recombination.[17,49] Furthermore, the shifting of the E_f level may also be one of the reasons for the enlarged V_{bi} which has been investigated in the Mott-Schottky plot. The minimised amount of PbI_2 residual on perovskite film can also reduce the metallic Pb formation and I_2 generation, which both have a detrimental impact on perovskite device performance and long-term stability.[49-52]

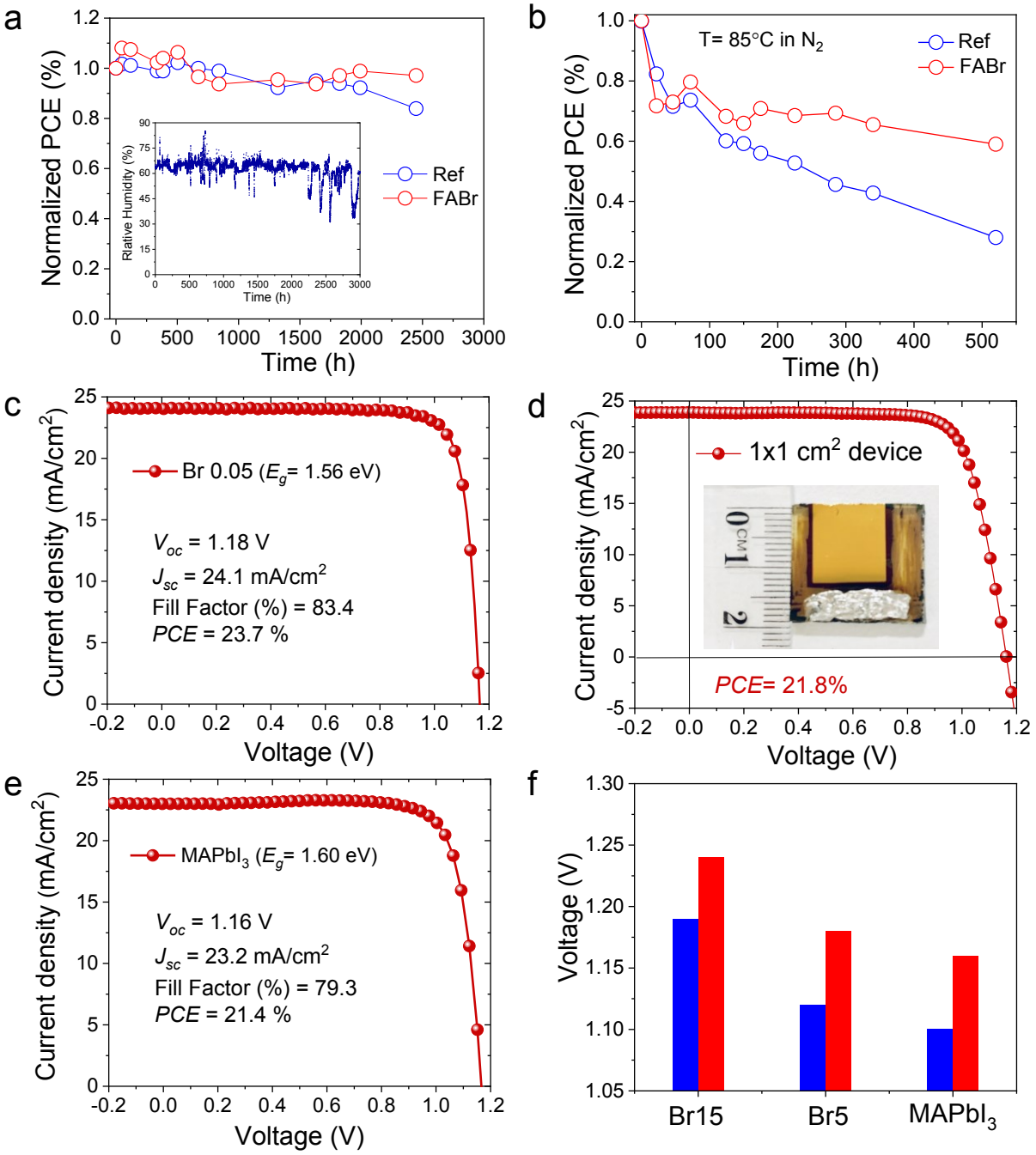

Figure 6. Device stability test for 1.63 eV bandgap perovskite and the universality of homologous FABr passivation in different bandgap perovskite solar cells. a) Stability test of reference and FABr passivated devices for 2500 hours under ambient (average relative humidity at 65% and

temperature of ~ 20°C) storage. Insert shows recorded humidity during the stability test. b) Thermal stability test at 85°C for 520 hours in N_2 atmosphere. c) The *J-V* curve of the best FABr passivated perovskite device with a perovskite bandgap of 1.56 eV and d) the best performance cell with the device area of 1×1 cm^2. e) The champing efficiency for $MAPbI_3$ perovskite cell by FABr passivation. f) The corresponding V_{oc} for different bandgap perovskite with and without FABr passivation.

Device stability of non-encapsulated devices in ambient (average relative humidity (RH) at 65% and temperature of ~ 20°C) was monitored for a period of 2500 hours. Results are shown in Figure 6a and Figure S26. The FABr passivated cell maintained 97% of its initial efficiency, while the reference cell maintained 84% of its initial efficiency at the end of 2500 hours of stability test. Thermal stability for the perovskite solar cells has also been investigated by continuously heating at 85°C for 520 hours. Here it is noted that we replaced the hole transporting material Spiro-OMeTAD with PTAA for thermal stability test and the devices were taken out of the N_2 glove box for *I-V* measurement in the ambient atmosphere (RH~ 80%) for about twenty minutes each time. We also measured the device stability under maximum power point tracking (MPPT) under standard AM 1.5G illumination with the total irradiance of 100 mW/cm^2 without encapsulation. The results shown in Figure S31 show that the passivated device maintained over 90% of its original efficiency while the reference cell only maintained around 80% after 300 minutes continuous tracking, demonstrating improved operation stability. Furthermore, from Figure 6b, we found the passivated device has a much better thermal stability and device efficiency maintained 59% of its original efficiency while the reference device only maintained 28%. The better stability of FABr passivated devices is likely to be due to suppression of the PbI_2 by the homologous FABr preventing the perovskite from degradation.[51,52]

In order to confirm the universality of the homologous bromide (e.g., FABr) passivation, we also fabricated two different bandgap perovskites, including the smaller 1.56 eV bandgap perovskite with the composition of $Cs_{0.05}FA_{0.80}MA_{0.15}Pb(I_{0.95}Br_{0.05})_3$ (Figure S27 & Figure S28) and 1.60 eV bandgap $MAPbI_3$ (Figure S29). We found that the FABr passivation can both enhance the cell efficiency with an improved V_{oc}. Our highest device efficiency for 1.56 eV bandgap achieved an efficiency of 23.7% on 0.159 cm^2 and 21.8% on 1×1 cm^2 area (Figure 6c-d) with a very small W_{oc} of 0.38 V. The perovskite solar cell based on $MAPbI_3$ also achieved an efficiency of 21.4% with an improved V_{oc} from 1.09 V to 1.16 V. (Figure 6e and Figure S30). We summarised the V_{oc} of the different bandgap perovskite solar cells in Figure 6f. A consistent trend of the V_{oc} improvement was displayed, confirming the homologous FABr passivation technique used in our study can be universally used in different bandgap perovskite solar cells.

Conclusion

In conclusion, we report a highly effective surface and bulk passivation for triple-cation mixed halide perovskite solar cells via surface treatment using homologous bromides and we compared the effectiveness of FABr, MABr and PEABr. Distinct to previous works that conclude surface bromides treatment by homologous bromides such as MABr forming a thin bromide-rich large-bandgap layer, our result shows that bromide can penetrate the perovskite film and increase the bromine content within the bulk. Our results also suggest that homologous FABr is the most effective passivating material which spontaneously increases bromine amount both at the surface and in the bulk evident by surface chemical changes in XPS, bulk chemical changes in TOF-SIMS and depth-resolved XPS

results. Slightly increased bandgap after bromide passivation was also confirmed by perovskite absorbance, device EQE and PL, consistent with the increased bromine amount in the bulk film. Variety of charge dynamic characterisations confirmed the effective passivation of the trap states such as the undercoordinated lead defects (Pb^0 and PbI_2) and halide vacancies both at the surface and in the bulk, resulting in significant non-radiative recombination suppression.

The best efficiencies of 22.1% with a superior V_{oc} of 1.24 V for a 1.63 eV (W_{oc}= 0.39 V) bandgap perovskite and 23.7% with an V_{oc} of 1.18 V for a 1.56 eV (W_{oc}= 0.38 V) bandgap perovskite were achieved on 0.159 cm^2. For large area devices, a 21.8% efficient cell was also achieved on 1×1 cm^2. The best device with 1.63 eV bandgap device maintained 97% of its initial efficiency after 2500 hours storage at high humidity atmosphere and 59% of its initial efficiency after 520 hours of 85°C thermal stability test in N_2 atmosphere. The use of homologous bromide surface treatment reported in our work is a simple and efficient way to improve both the voltage and device efficiency of perovskite solar cells. Our work will not only be beneficial for improving the voltage of single-junction perovskite cells but may also shed light on developing other high performance optoelectronic devices, including perovskite-based tandems and light-emitting diodes (LEDs).

Experimental Section

Precursor preperation: Lead iodide (PbI_2) is from *Sigma-Aldrich*. Lead bromide ($PbBr_2$), caesium iodide (CsI), caesium bromide (CsBr), anhydrous N, N-dimethylformamide (DMF) and dimethyl sulfoxide (DMSO) are from *Alfa Aesar*. Formamidinium iodide (FAI), Formamidinium bromide (FABr) and methylammonium bromide (MABr) are from *Greatcell Solar*. All chemicals were used as received

without any further purification. The perovskite precursors were prepared by using a composition of $Cs_{0.05}FA_{0.80}MA_{0.15}Pb(I_{1-x}Br_x)_3$. (x=0.15 or 0.05). The precursors containing ~1.4 M perovskite were prepared by mixing into 1 ml mixed solvents (DMF: DMSO=4:1).

Device fabrication: The device structure is FTO/*c*-TiO_2/*mp*-TiO_2/perovskite/bromides passivation layer/Spiro-OMeTAD/Au. Firstly, the FTO substrate was pre-cleaned by 2% Hellmanex detergent, acetone, isothanol and ethanol, respectively. The substrates were then treated by ultraviolet ozone (UVO) for 10 minutes. Then the compact TiO_2 (*c*-TiO_2) was deposited by spray pyrolysis (~50 nm) using 300 mM titanium diisopropoxide bis(acetylacetonate) solution at 500 °C on the clean FTO glass in the ambient atmosphere. After cooling down to room temperature, the mesoporous TiO_2 (*mp*-TiO_2) layer was then deposited by spin-coating a diluted Dyesol 30-NR TiO_2 paste in ethanol at 135 mg/ml at 4000 rpm onto the *c*-TiO_2 layer. Then, the films were annealed at 100 °C for 10 mins, followed by sintering at 500 °C for 30 mins in a muffle furnace. After cooling down, the substrates were then transferred into a nitrogen filled glovebox (both O_2 and H_2O < 2.0 ppm). For the perovskite deposition, a 50 µl ~1.4 M perovskite precursor solution was spin-coated onto the *mp*-TiO_2 layer at 2000 rpm for 10s (acceleration rate at 200 rpm/s) and 4000 rpm for 30 s (acceleration rate at 2000 rpm/s). During the second stage of the spin-coating (high speed) process, the anti-solvent chlorobenzene was dripped (at 20 seconds) onto the perovskite surface. The as-deposited perovskite films were then left drying naturally for five minutes in a capped petri dish and were subsequently annealed at 100 °C for 10 minutes, during which the colour of the films converted from brown to black. After being cooled down to the room temperature, different bromide passivation materials (e.g., 5 mg/ml FABr solution in IPA) was spin-coated on the perovskite surface to form a passivation layer. Noted here the passivation solution was quickly drop on the film to cover the

whole perovskite area and waiting for 3 seconds before started the spinning. It is noticed that waiting too long or too short period will influence the passivation effect. The final passivation layer was formed by thermal annealing at 100°C for 5 mins to fully remove the IPA solvent. For the hole transport layer, a Spiro-OMeTAD solution containing 72.3 mg of Spiro-OMeTAD, 35 µl of 260 mg/ml lithium salt in acetonitrile and 30 µl 4-tert-butylpyridine in 1 ml chlorobenzene was spin-coated onto the perovskite at 3000 rpm for 30 s. Finally, 100 nm thick Au cathode was deposited by thermal vacuum evaporation under 10^{-6} Torr. No antireflection coating has been used in our device fabrication.

Characterisations: The current density-voltage (*J-V*) parameters of the devices were characterised by using a Keithley 2400 digital source meter under the simulated AM 1.5G solar irradiation (ABET 3000, Class AAA Solar Simulator) at 100 mW cm^{-2}. The light intensity is calibrated by a certified silicon reference cell (Fraunhofer ISE, RSID-5). An aperture of 0.159 cm^2 is used during the *J-V* measurements. Note that reverse scan is from V_{oc} to J_{sc} (1.2-1.3 V → -0.2 V) and forward scan is from J_{sc} to V_{oc} (-0.2 V → 1.2-1.3 V), with the scan speed of 50 mV s^{-1}. No preconditioning protocol and no additional filters were applied for the *J-V* the measurement. EQE measurement was carried out using the PV Measurement QXE7 Spectral Response system with monochromatic light from a xenon arc lamp.

The ultraviolet-visible spectroscopy (UV-*vis*) spectra were measured by a Perkin Elmer model Lambda 1050 instrument. Steady-state photoluminescence (PL) measurement of films was conducted using Andor iVac CCD detector (detector temperature is -60 °C). The excitation wavelength was 409 nm and the signal was collected under one second exposure time.

CWPL measurements were performed using an in-house micro-photoluminescence microscope. Optical excitation was achieved using an LED with a centre wavelength of 525 nm in the epi-illumination configuration. A short pass 575 nm filter was placed in the excitation path to remove the low-energy tail emission of the LED. This was focussed on the sample using a 0.6 NA, 50× magnification refractive lens, resulting in an incident light intensity of approximately 1 W/cm^2 and 600 µm diameter spot-size. The PL emission was passed through 600 nm long-pass filters to remove reflected optical excitation, followed by coupling into a 500 µm diameter, 0.22 NA multimode optical fibre. A silicon charge-coupled device spectrometer detected the PL emission relayed from the optical fibre.

Conventional XRD measurement was conducted using a PANalytical 80 equipment (Empyrean, Cu Ka radiation) at 45 kV and 40 mA. Top-view and cross-sectional SEM images were obtained using a field emission SEM (NanoSEM 450). GIWAX was measured by using the Xeuss 3.0 from Xenocs. Ga was used as the light source with a wavelength of 1.341A, with an exposure time of 300s and SD of 250 mm.

AFM measurements were performed by the Bruker Dimension ICON SPM with a Nanoscope V controller. A platinum-iridium coated AFM tip (SCMPIT-V2, Bruker AFM probes) was used to scan the surface. Amplitude modulated KPFM (AM-KPFM) measurement was performed using the Bruker Dimension ICON SPM with a Nanoscope V controller. A platinum-iridium coated AFM tip (SCM-PIT-V2, Bruker AFM probes) was used to scan the surface. Then the perovskite film was scanned with a small bias voltage applied for the actual measurement.

Intensity-dependent-PL, voltage-dependent EL and voltage-dependent PL for device $PLQE_{OC-SC}$ measurements under open-circuit (OC) and short-circuit (SC) conditions were operated on a FL 1039 spectrometer from Horiba Scientific. Different illumination conditions were achieved by using a continuous wavelength 635 nm laser (generated by a commercial laser diode purchased from Thorn labs) through a focus lens and varying transmittance neutral dense filters. 1 Sun equivalent illumination was calibrated by matching the current of the device under laser to its J_{sc}. A long pass filter after 675 nm was finally used before the spectrometer to avoid scattered laser light entering the spectrometer. Time-resolved photoluminescence was measured using time-correlated single photon counting (TCSPC) fluorescence lifetime system (Horiba Jobin Yvon, FluoroCube) with the excitation wavelength of 470 nm.

The XPS was carried out with an X-ray source of monochromated Al Kα (energy 1486.68 eV) with the power of 160W (14.5 × 11 mA) using ESCALAB250Xi, Thermo Scientific, UK. The UPS measurement was carried out with the ultraviolet source He I (energy 21.2eV) and pass energy of 2 eV at the background vacuum below $2x10^{-9}$ mbar. XPS depth profiles were obtained by using Ar ion beam of 1 keV to etch the perovskite surface (etched area 2.5 mm × 2.5 mm).

TOF-SIMS analysis was carried out in positive polarity by Bi^{3+} at 30 KeV, sputtered by Cs^{+} beam of 0.5 keV, in MCs mode. PYS measurements were conducted with a photoelectron emission yield spectrometer (Riken Keiki, AC-3E).

Electrochemical impedance spectra (EIS) of the devices were measured under the illumination of 500 nm LED by ModuLab XM PhotoEchem from Solartron Analytical, UK. Mott-Schottky plot and thermal admittance spectroscopy was also obtained by ModuLab XM PhotoEchem from Solartron Analytical,

UK. The capacitance-frequency spectra of the device were measured by scanning the frequency from 1Hz to 100 kHz at room temperature in the dark.

Supporting Information

Supporting Information is available from the Wiley Online Library or from the author.

Acknowledgements

The Australian Centre for Advanced Photovoltaics (ACAP) encompasses the Australian based activities of the Australia-US Institute for Advanced Photovoltaics (AUSIAPV) and is supported by the Australian Government through the Australian Renewable Energy Agency (ARENA). Y.L. thank the surface analysis laboratory (SSEAU), Electron Microscopy Unit (EMU) and the Biomedical Imaging Facility at UNSW. W. X. would like to thank the financial support from China Scholarship Council (CSC) and SUNRISE project (EP/P032591/1).

Conflict of Interest

The authors declare no conflict of interest.

Author Contributions

Y.L., W.X. and N. M. contributed equally to this work. Y.L. designed the whole experiment, fabricated the device and conduct most of the characterisation and analysis. W.X. did the $PLQE_{OC-SC}$ and EL characterisations. N. M. did the CWPL measurement and helped the long-term stability measurement. Y.C. did with the TRPL and PYS characterisations. J. B. helped draw the passivation mechanism image. Q. Z. conducted the GIWAX characterisation. The manuscript was written by Y.L. and revised by S.H. through contributions from all authors.

Keywords

perovskite solar cell, surface passivation, high efficiency, V_{oc} loss

Received: ((will be filled in by the editorial staff))
Revised: ((will be filled in by the editorial staff))
Published online: ((will be filled in by the editorial staff))

References

[1] A. Kojima, K. Teshima, Y. Shirai, and T. Miyasaka, *Journal of the American Chemical Society* **2009**, *131*, 6050-6051.

[2] H.-S. Kim, C.-R. Lee, J.-H. Im, K.-B. Lee, T. Moehl, A. Marchioro, S.-J. Moon, R. Humphry-Baker, J.-H. Yum, J.E. Moser, M. Grätzel, N.-G. Park, *Scientific Reports* **2012**, *2*, 591.

[3] M.M. Lee, J. Teuscher, T. Miyasaka, T.N. Murakami, H.J. Snaith, *Science* 2012, *338*, 643-647.

[4] M.A. Green, A. Ho-Baillie, H.J. Snaith, *Nature Photonics* **2014**, *8*, 506-514.

[5] The latest NREL efficiency chart, *https://www.nrel.gov/pv/cell-efficiency.html*

[6] K.X. Steirer, P. Schulz, G. Teeter, V. Stevanovic, M. Yang, K. Zhu, J.J. Berry, *ACS Energy Letters* 2016, *1*, 360-366.

[7] W. Shockley, H.J. Queisser, *Journal of Applied Physics* **1961**, *32*, 510-519.

[8] J.-P. Correa-Baena, M. Saliba, T. Buonassisi, M. Grätzel, A. Abate, W. Tress, A. Hagfeldt, *Science* **2017**, *358*, 739-744.

[9] I.L. Braly, D.W. deQuilettes, L.M. Pazos-Outón, S. Burke, M.E. Ziffer, D.S. Ginger, H.W. Hillhouse,*Nature Photonics* **2018**, *12*, 355-361.

[10] J. Peng, Y. Wu, W. Ye, D.A. Jacobs, H. Shen, X. Fu, Y. Wan, T. Duong, N. Wu, C. Barugkin, H.T. Nguyen, D. Zhong, J. Li, T. Lu, Y. Liu, M.N. Lockrey, K.J. Weber, K.R. Catchpole, T.P. White, *Energy & Environmental Science* **2017**, *10*, 1792-1800.

[11] D. Bi, C. Yi, J. Luo, J.-D. Décoppet, F. Zhang, Shaik M. Zakeeruddin, X. Li, A. Hagfeldt, M. Grätzel, *Nature Energy* **2016**, *1*, 16142.

[12] J. Xu, A. Buin, A.H. Ip, W. Li, O. Voznyy, R. Comin, M. Yuan, S. Jeon, Z. Ning, J.J. McDowell, P. Kanjanaboos, J.P. Sun, X. Lan, L.N. Quan, D.H. Kim, I.G. Hill, P. Maksymovych, E.H. Sargent, *Nature communications* **2015**, *6*, 7081.

[13] F. Zhang, W. Shi, J. Luo, N. Pellet, C. Yi, X. Li, X. Zhao, T.J.S. Dennis, X. Li, S. Wang, Y. Xiao, S.M. Zakeeruddin, D. Bi, M. Grätzel, *Advanced Materials* **2017**, *29*, 1606806.

[14] C.-H. Chiang, C.-G. Wu, Bulk heterojunction perovskite–PCBM solar cells with high fill factor, *Nature Photonics* **2016**, *10*, 196-200.

[15] J. Peng, J.I. Khan, W. Liu, E. Ugur, T. Duong, Y. Wu, H. Shen, K. Wang, H. Dang, E. Aydin, X. Yang, Y. Wan, K.J. Weber, K.R. Catchpole, F. Laquai, S. De Wolf, T.P. White, *Advanced Energy Materials* **2018**, *8,* 1801208.

[16] N.K. Noel, A. Abate, S.D. Stranks, E.S. Parrott, V.M. Burlakov, A. Goriely, H.J. Snaith,*ACS Nano* **2014**, *8*, 9815-9821.

[17] D.W. de Quilettes, S.M. Vorpahl, S.D. Stranks, H. Nagaoka, G.E. Eperon, M.E. Ziffer, H.J. Snaith, D.S. Ginger, *Science* **2015**, *348*, 683-686.

[18] E. Aydin, M. De Bastiani, S. De Wolf, *Advanced Materials* **2019**, *31*, 1900428.

[19] D. Luo, W. Yang, Z. Wang, A. Sadhanala, Q. Hu, R. Su, R. Shivanna, G.F. Trindade, J.F. Watts, Z. Xu, T. Liu, K. Chen, F. Ye, P. Wu, L. Zhao, J. Wu, Y. Tu, Y. Zhang, X. Yang, W. Zhang, R.H. Friend, Q. Gong, H.J. Snaith, R. Zhu, *Science* **2018**, *360*, 1442-1446.

[20] Q. Jiang, Y. Zhao, X. Zhang, X. Yang, Y. Chen, Z. Chu, Q. Ye, X. Li, Z. Yin, J. You, *Nature Photonics* **2019**, *13*, 460-466.

[21] E.H. Jung, N.J. Jeon, E.Y. Park, C.S. Moon, T.J. Shin, T.Y. Yang, J.H. Noh, J. Seo, *Nature* 2019, *567*, 511-515.

[22] J.J. Yoo, S. Wieghold, M.C. Sponseller, M.R. Chua, S.N. Bertram, N.T.P. Hartono, J.S. Tresback, E.C. Hansen, J.-P. Correa-Baena, V. Bulović, T. Buonassisi, S.S. Shin, M.G. Bawendi, *Energy & Environmental Science* **2019**, *12*, 2192-2199.

[23] M. Yang, T. Zhang, P. Schulz, Z. Li, G. Li, D.H. Kim, N. Guo, J.J. Berry, K. Zhu, Y. Zhao, *Nature communications* **2016**, *7*, 12305.

[24] G. Han, T.M. Koh, S.S. Lim, T.W. Goh, X. Guo, S.W. Leow, R. Begum, T.C. Sum, N. Mathews, S. Mhaisalkar, *ACS applied materials & interfaces* **2017**, *9*, 21292-21297.

[25] Z. Hu, Q. An, H. Xiang, L. Aigouy, B. Sun, Y. Vaynzof, Z. Chen, *ACS applied materials & interfaces* **2020**, *12*, 54824-54832.

[26] F. Fu, S. Pisoni, T.P. Weiss, T. Feurer, A. Wackerlin, P. Fuchs, S. Nishiwaki, L. Zortea, A.N. Tiwari, S. Buecheler, *Advanced Science* **2018**, *5*, 1700675.

[27] K.T. Cho, S. Paek, G. Grancini, C. Roldán-Carmona, P. Gao, Y. Lee, M.K. Nazeeruddin, *Energy & Environmental Science* **2017**, *10*, 621-627.

[28] M. Saliba, T. Matsui, J.Y. Seo, K. Domanski, J.P. Correa-Baena, M.K. Nazeeruddin, S.M. Zakeeruddin, W. Tress, A. Abate, A. Hagfeldt, M. Gratzel, *Energy Environ Sci* **2016**, *9*, 1989-1997.

[29] Y. Li, J. Shi, J. Zheng, J. Bing, J. Yuan, Y. Cho, S. Tang, M. Zhang, Y. Yao, C.F.J. Lau, D.S. Lee, C. Liao, M.A. Green, S. Huang, W. Ma, A.W.Y. Ho-Baillie, *Advanced Science* **2020**, *7*, 1903368.

[30] B. Conings, J. Drijkoningen, N. Gauquelin, A. Babayigit, J. D'Haen, L. D'Olieslaeger, A. Ethirajan, J. Verbeeck, J. Manca, E. Mosconi, F.D. Angelis, H.-G. Boyen, *Advanced Energy Materials* **2015**, *5*, 1500477.

[31] R.K. Misra, S. Aharon, B. Li, D. Mogilyansky, I. Visoly-Fisher, L. Etgar, E.A. Katz, *The Journal of Physical Chemistry Letters* **2015**, *6*, 326-330.

[32] G.E. Eperon, S.D. Stranks, C. Menelaou, M.B. Johnston, L.M. Herz, H.J. Snaith, *Energy & Environmental Science* **2014**, *7*, 982.

[33] W.S. Yang, J.H. Noh, N.J. Jeon, Y.C. Kim, S. Ryu, J. Seo, S.I. Seok, *Science* **2015**, *348*, 1234.

[34] C.C. Stoumpos, C.D. Malliakas, M.G. Kanatzidis, *Inorg. Chem.* **2013**, *52*, 9019-9038.

[35] S. Dastidar, C.J. Hawley, A.D. Dillon, A.D. Gutierrez-Perez, J.E. Spanier, A.T. Fafarman, *J. Phys. Chem. Lett.* **2017**, *8*, 1278-1282.

[36] A. Ho-Baillie, M. Zhang, C.F.J. Lau, F.-J. Ma, S. Huang, *Joule* **2019**, *3*, 938-955.

[37] G. Sadoughi, D.E. Starr, E. Handick, S.D. Stranks, M. Gorgoi, R.G. Wilks, M. Bar, H.J. Snaith, *ACS applied materials & interfaces* **2015**, *7*, 13440.

[38] Y. Cho, A.M. Soufiani, J.S. Yun, J. Kim, D.S. Lee, J. Seidel, X. Deng, M.A. Green, S. Huang, A.W.Y. Ho-Baillie, Adv. *Energy Mater.* **2018**, *8*, 1703392.

[39] J. Fang, Z. Ding, X. Chang, J. Lu, T. Yang, J. Wen, Y. Fan, Y. Zhang, T. Luo, Y. Chen, S. Liu, K. Zhao, *Journal of Materials Chemistry A,* **2021**, *9*, 13297-13305.

[40] T. Du, W. Xu, M. Daboczi, J. Kim, S. Xu, C.-T. Lin, H. Kang, K. Lee, M.J. Heeney, J.-S. Kim, J.R. Durrant, M.A. McLachlan, *Journal of Materials Chemistry A* **2019**, *7*, 18971-18979.

[41] Z. Liu, L. Krückemeier, B. Krogmeier, B. Klingebiel, J.A. Márquez, S. Levcenko, S. Öz, S. Mathur, U. Rau, T. Unold, T. Kirchartz, *ACS Energy Letters* **2019**, *4*, 110-117.

[42] P. Caprioglio, M. Stolterfoht, C.M. Wolff, T. Unold, B. Rech, S. Albrecht, D. Neher, *Advanced Energy Materials* **2019**, *9*, 1901631.

[43] J. Kim, R. Godin, S.D. Dimitrov, T. Du, D. Bryant, M.A. McLachlan, J.R. Durrant, *Advanced Energy Materials* **2018**, *8*, 1802474.

[44] G. Zheng, C. Zhu, J. Ma, X. Zhang, G. Tang, R. Li, Y. Chen, L. Li, J. Hu, J. Hong, Q. Chen, X. Gao, H. Zhou, *Nature communications* **2018**, *9*, 2793.

[45] T. He, S. Li, Y. Jiang, C. Qin, M. Cui, L. Qiao, H. Xu, J. Yang, R. Long, H. Wang, M. Yuan, *Nature communications* **2020**, *11*, 1672.

[46] C.C. Zhang, Z.K. Wang, S. Yuan, R. Wang, M. Li, M.F. Jimoh, L.S. Liao, Y. Yang, *Adv Mater,* 2019, e1902222.

[47] X. Zheng, B. Chen, J. Dai, Y. Fang, Y. Bai, Y. Lin, H. Wei, Xiao C. Zeng, J. Huang, *Nature Energy* **2017**, *2*, 17102.

[48] J. M. Ball, A. Petrozza, *Nature Energy* **2016**, *1*, 16149.

[49] C. Quarti, F. De Angelis, D. Beljonne, *Chemistry of Materials* **2017**, *29*, 958-968.

[50] F. Liu, Q. Dong, M.K. Wong, A.B. Djurišić, A. Ng, Z. Ren, Q. Shen, C. Surya, W.K. Chan, J. Wang, A.M.C. Ng, C. Liao, H. Li, K. Shih, C. Wei, H. Su, J. Dai, *Advanced Energy Materials* **2016**, *6*, 1502206.

[51] F. Fu, S. Pisoni, Q. Jeangros, J. Sastre-Pellicer, M. Kawecki, A. Paracchino, T. Moser, J. Werner, C. Andres, L. Duchêne, P. Fiala, M. Rawlence, S. Nicolay, C. Ballif, A.N. Tiwari, S. Buecheler, *Energy & Environmental Science* **2019**, *12*, 3074-3088.

[52] G. Tumen-Ulzii, C. Qin, D. Klotz, M.R. Leyden, P. Wang, M. Auffray, T. Fujihara, T. Matsushima, J.-W. Lee, S.-J. Lee, Y. Yang, C. Adachi, *Advanced Materials* **2020**, *32*, 1905035.

Table of Contents (ToC) :

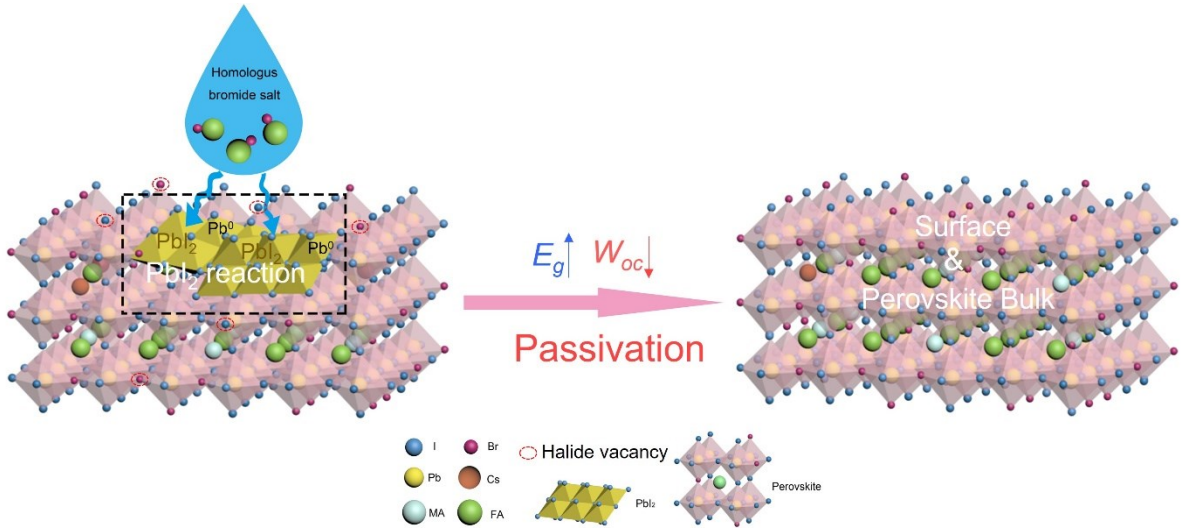

Text:

This work provides a thorough investigation of the perovskite surface treatment by homologous bromide salts. It is found that bromides not only passivate surface defects but also penetrate into the perovskite providing bulk passivation. This leads to a large voltage of 1.24 V in a 1.63 eV bandgap device and an efficiency of 23.7% in a 1.56 eV bandgap device.